Proceedings of the ASME 2026 21st International Manufacturing Science and Engineering Conference MSEC2026 June 14–18, 2026, State College, Pennsylvania

MSEC2026-182721

DESIGN AND MULTI-AXIS ADDITIVE MANUFACTURING OF LIGHTWEIGHT AND SKIN-COMPATIBLE MESH SPLINTS USING CONTINUOUS BASALT FIBER FOR REHABILITATION

Fang Li[1], Feiyang Gao[1], Yuexin Yang[1], Yi Zhou[1], Molong Duan[1,2,*]

[1]Hong Kong University of Science and Technology, Hong Kong SAR, China
[2]HKUST Shenzhen-Hong Kong Collaborative Innovation Research Institute, Futian, Shenzhen, China

ABSTRACT

Rehabilitation splints are external supports designed to stabilize injured joints while maintaining daily comfort. Conventional splints are typically made from isotropic thermoplastics through thermoforming or injection molding, producing dense, uniform-thickness parts that lack air permissibility and customization, limiting potential mechanical performance and long-term comfort. While continuous fiber-reinforced thermoplastic composites integrated with multi-axis additive manufacturing (AM) offer a promising pathway to lightweight, breathable, and customized splints, a significant gap remains. Existing fiber path generation tools focus predominantly on mechanical performance, failing to establish a joint consideration of structural compliance and skin compatibility. To address this, we present an integrated design and manufacturing approach that leverages basalt fiber/PLA composites, multi-objective fiber-path optimization, and multi-axis AM. The process begins with reconstructing a patient-specific splint geometry. Finite element analysis then guides the alignment of continuous fibers according to the stress field, creating an optimized, lightweight lattice structure that balances strength with comfort. This design is fabricated using a multi-axis AM system equipped with a robotic arm and a co-extrusion nozzle to precisely deposit fibers onto the complex curved substrate. A finger-splint prototype validated the method, with simulations and experiments confirming that the design provides reliable mechanical strength for fixation while significantly improving breathability. This work establishes a practical and sustainable framework for developing next-generation, high-performance rehabilitation devices.

Keywords: Continuous fiber-reinforced thermoplastic composites (CFRTPCs); Multi-axis additive manufacturing; Fiber-path optimization; Rehabilitation devices.

1. INTRODUCTION

Musculoskeletal injuries can occur in a wide range of joints, including major load-bearing joints such as the knee and wrist as well as smaller peripheral articulations such as the phalangeal joints [1]. During rehabilitation, external stabilization is frequently required to support proper tissue healing, maintain joint alignment, and prevent secondary deformation. Rehabilitation splints therefore serve as essential devices that restrict undesired motion while enabling the controlled recovery of functional mobility [2]. The design of rehabilitation orthoses requires a careful balance between mechanical stiffness, which provides motion restriction, and long-term wearing comfort to ensure physiological adaptability. Conventional orthoses fabricated from homogeneous thermoplastics such as polyethylene or polylactic acid (PLA) often exhibit poor breathability, thermal accumulation, and inadequate anatomical conformity, which can gradually lead to skin irritation, moisture retention, and reduced patient compliance [3-5]. Developing a mechanically robust, breathable, and biocompatible composite system has therefore become essential for the next generation of personalized rehabilitation supports.

To address these functional and physiological requirements, material development plays a foundational role. Basalt-fiber-reinforced PLA composites have demonstrated outstanding potential in terms of both mechanical performance and environmental sustainability [6][7]. Jagadeesh et al. [8] reported that basalt fibers, derived from natural volcanic rock, possess

* Corresponding author: duan@ust.hk

high tensile strength, superior thermal stability, and strong corrosion resistance, while their production process is simple, non-toxic, and pollution-free, yielding excellent environmental compatibility and skin safety. Subsequent work showed that incorporating basalt fibers into a PLA matrix improves stiffness, dimensional stability, and heat resistance while retaining the polymer’s biodegradability and recyclability. Hassan et al. [9] verified through studies on basalt-fiber-reinforced polymer (BFRP) beams that these composites exhibit high specific strength and chemical inertness, confirming their feasibility for sustainable structural applications. These combined characteristics make basalt/PLA composites particularly suitable for splints that must simultaneously provide mechanical protection and long-term wearing comfort.

Material innovation alone cannot fully address the ergonomic and functional requirements of splints. To achieve efficient load transfer and user comfort, structural optimization is also necessary, especially through the use of continuous fibers that can align with physiological load paths. Continuous reinforcement enables anisotropic strengthening, reduces unnecessary material usage, and better matches the stress distribution experienced by the human joint. Stress-guided fiber-path optimization therefore provides a compelling framework for integrating load-bearing performance with breathable and compliant structural design [10]. In terms of structural optimization, stress-guided fiber-path algorithms have been shown to markedly enhance the load-bearing efficiency of continuous-fiber composites [11][12]. Liu et al.[13] developed a stress-driven infill mapping algorithm based on finite-element stress analysis, combining wave-projection and traveling-salesman frameworks to generate continuous fiber trajectories aligned with the principal stress gradient direction, thereby minimizing discontinuities and voids. Medeghini et al. [14] validated this principle in full-scale concrete plates, demonstrating that fibers aligned along principal tensile-stress gradients significantly improved crack control and load-carrying capacity. These findings confirm that stress-field-driven fiber orientation can achieve anisotropic reinforcement consistent with local stress distributions. With the advancement of multi-axis additive manufacturing, such gradient-conforming fiber architectures can now be fabricated with high spatial precision, ensuring continuous deposition across complex geometries [15][16].

Nevertheless, despite the verified performance of stress-guided optimization and basalt-based composites in engineering applications, their integration for biomedical and rehabilitative orthoses remains largely unexplored. Interdisciplinary coupling among materials science, computational path optimization, and multi-axis additive manufacturing has yet to be systematically addressed. To bridge this gap, the present work combines a recyclable, biocompatible basalt/PLA composite system with a stress-guided fiber-trajectory optimization algorithm, implemented through multi-axis additive manufacturing for the design and fabrication of personalized orthoses. The framework orients continuous fibers along finite-element-derived stress gradients to realize lightweight, efficient, and ventilated composite structures. A customized orthosis for the proximal phalanx of the little finger served as a case study. Variants with different materials and layouts are fabricated and experimentally evaluated. The optimized design maintained stiffness while substantially reducing material usage and enhancing ventilation. By integrating sustainable materials with stress-driven structural design, the approach enables high-performance, environmentally responsible, patient-specific additive manufacturing of rehabilitation devices.

2. MATERIALS AND METHODS

To facilitate understanding of the integrated workflow, FIGURE 1 provides a summarized representation of the complete design-to-fabrication process, encompassing material preparation, path optimization, multi-axis additive manufacturing, and performance evaluation.

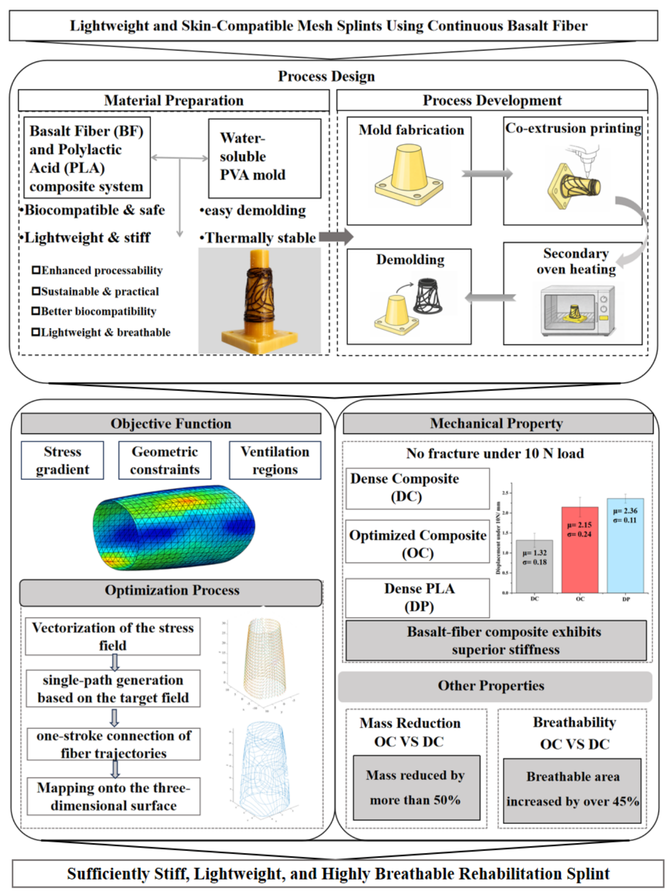

FIGURE 1: WORKFLOW DIAGRAM

2.1 Materials

The primary materials adopted in this study are basalt fiber (BF) and polylactic acid (PLA), which respectively represent a robust inorganic reinforcement and a renewable thermoplastic matrix. Basalt fiber is manufactured by melting and drawing natural volcanic rock without chemical additives, resulting in a material that combines high mechanical integrity, thermal stability, and chemical inertness with a comparatively low density. Its inorganic origin also imparts favorable skin compatibility and resistance to allergenic reactions, making it suitable for long-term wear in rehabilitation splints. Owing to these characteristics, basalt fiber has been increasingly utilized as an alternative to carbon and glass fibers in engineering applications and has shown emerging potential in biomechanical and orthotic devices.

PLA serves as the matrix polymer and offers an environmentally sustainable route through its derivation from plant-based feedstocks. As a biodegradable thermoplastic with reliable processing behavior, PLA can be readily shaped or extruded under mild thermal conditions while maintaining adequate stiffness and dimensional stability. Its established biocompatibility has enabled widespread use in biomedical fixation devices and soft orthotic supports. Although PLA is advantageous in manufacturability and recyclability, conventional PLA splints often exhibit limited breathability and accumulate heat during extended wear, motivating performance improvements through reinforcement or structural redesign.

From the perspective of material pairing, basalt fiber and PLA provide complementary benefits: the fiber contributes strength and thermal resistance, while the polymer ensures processability and comfort. Their combination thus establishes a sustainable composite system capable of supporting both mechanical reliability and skin compatibility. TABLE 1 summarizes the representative material characteristics used in this work.

TABLE 1 Basic properties of materials

Property	Basalt Fiber (BF)	PLA (neat)
Density ($g \cdot cm^{-3}$)	2.6 – 2.8	1.22 – 1.28
Tensile strength (MPa)	3000 – 3400	55 – 70
Tensile modulus (GPa)	85 – 100	3.0 – 3.5
Elongation at break (%)	2.5 – 3.2	3 – 6
Biocompatibility	Inert, non-allergenic (no toxic additives)	Depending on formulation
Sustainability	Natural origin, simple processing	Renewable, recyclable

2.2 Experimental Setup and Model Construction

The fabrication process was conducted on an integrated multi-axis printing system, as shown in FIGURE 2. The system consists of a six-degree-of-freedom robotic arm and a printing head equipped with independent temperature and material-flow control. The printing head is mounted on a fixed truss frame, while the forming mold is attached to the sixth joint of the robotic arm. For composite fabrication, a 0.8 mm nozzle was employed, with PLA serving as the matrix material and dry continuous basalt fiber (0.4K) used as the reinforcement phase. The nozzle temperature was maintained at 220 °C, and the fiber printing velocity was set to 3 mm/s, as shown in Table 2. These parameters define the processing conditions of the BF/PLA composite strand during multi-axis deposition. During deposition, the extrusion motor feeds the filament into the heating zone at a constant rate, and the nozzle temperature is maintained at 220–230 °C to ensure stable and continuous extrusion of the molten composite. This configuration enables controlled deposition of continuous fibers on complex curved surfaces and provides a versatile platform for multi-axis additive manufacturing of non-planar geometries.

TABLE 2 Parameters of multi-axis platform.

Parameter	Values
Nozzle diameter	0.8 mm
Matrix material	PLA
Continuous fiber	0.4 K basalt fiber
Nozzle temperature	220 ℃
Printing velocity	3 mm/s
Maximum curvature	0.6 mm^{-1}

Compared with conventional Cartesian three-axis printers, the proposed multi-axis robotic platform dynamically adjusts the nozzle orientation according to the local path normal during printing, maintaining perpendicularity between the nozzle and the surface at all times. This capability markedly reduces the risk of fiber fracture and material accumulation at turning points. It also improves geometric precision, surface uniformity, and deposition continuity, thereby avoiding local stress concentration. Through synchronized motion control, the system achieves continuous fabrication on complex spatial surfaces and is particularly suited for stress-guided fiber deposition. The cooperative motion between the robotic arm and the print head enables the formation of uninterrupted toolpaths on non-planar surfaces, significantly enhancing structural integration and geometric freedom.

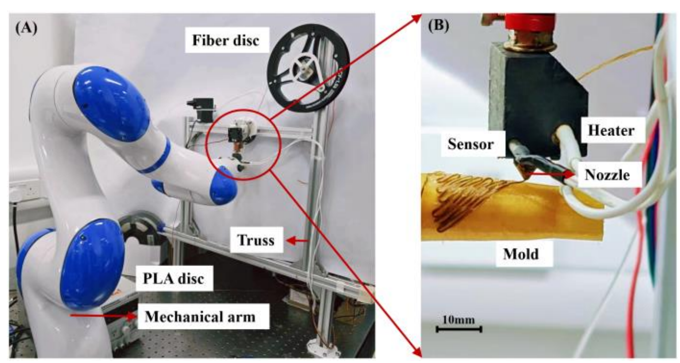

FIGURE 2: MULTI-AXIS PRINTING PLATFORM AND PRINTING HEAD

To validate the functionality and feasibility of the system, a proximal phalanx orthotic splint for the little finger was selected as a representative model. The little finger is one of the most injury-prone digits of the hand, frequently affected by tendon and ligament damage. Its cross-sectional variation and pronounced curvature provide an effective benchmark for assessing both shape adaptability and path complexity. As illustrated in FIGURE 3(A), the designed finger-sleeve structure features irregular and dissimilar upper and lower cross-sections. Based on anatomical data, an individualized three-dimensional model was reconstructed, and corresponding orthosis and mold geometries were generated in CAD software to verify the accuracy of personalized modeling and toolpath planning.

The forming mold was printed using water-soluble polyvinyl alcohol (PVA) via fused-filament deposition. PVA provides excellent surface quality and thermal stability and can be readily dissolved in water after printing, making it suitable for the fabrication of complex internal or closed-surface geometries. As shown in FIGURE 3(B), the mold was clamped to the robotic arm’s end effector to implement a “mold-following printing” configuration, wherein the arm drives the mold’s motion while the print head remains fixed in orientation to complete the deposition. This strategy effectively eliminates nozzle interference caused by abrupt path transitions and ensures smooth fiber placement along the surface while preserving the stress-aligned characteristics of the trajectory.

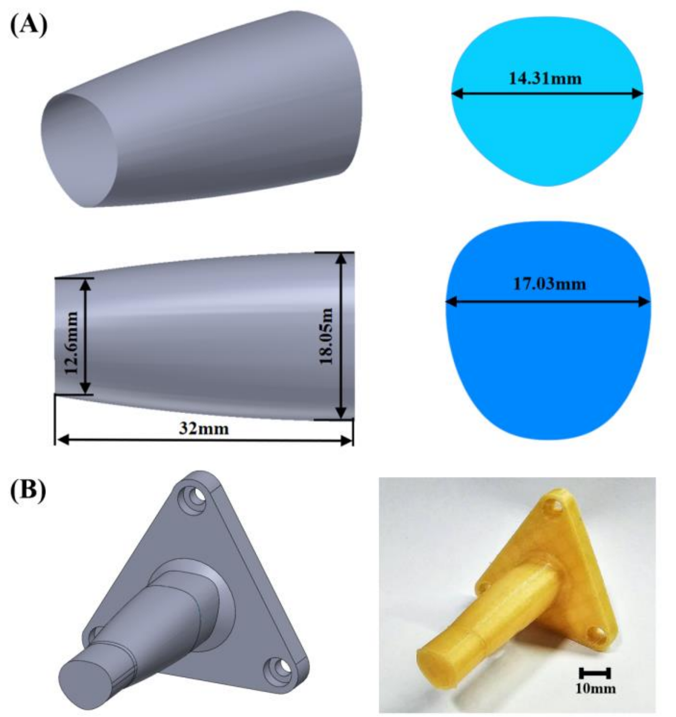

FIGURE 3: FINGER SPLINTS AND MOLD MODELS. (A) DRAWING OF FINGER SPLINTS; (B) MOLD OF FINGER SPLINTS.

Upon completion, the printed component underwent secondary thermal treatment at 80°C for 3 hours in a convection oven to enhance fiber–matrix interfacial bonding and to relieve residual thermal stress accumulated during deposition. After natural cooling, the part together with its PVA mold was immersed in 40 °C deionized water for dissolution and demolding, yielding a fully formed orthotic splint with a smooth surface finish.

2.3 Path Optimization Strategy

To achieve a rehabilitation splint structure that simultaneously provides load-bearing capability and breathability, this study extends the conventional stress-guided continuous-fiber optimization algorithm [17]. Using finite-element analysis (FEA), the stress distribution of the target component is first determined, and continuous fiber paths are then generated along the principal-stress gradient to achieve directional reinforcement. The three-dimensional splint model is quasi-conformally mapped onto a two-dimensional parametric domain, preserving local angular relationships while introducing a length-distortion factor for subsequent path-density compensation. The mapped principal-stress field is converted into a continuous vector field, and path planning is reformulated as the search for curves consistent with the local principal-stress gradient. To avoid the numerical instability of direct path integration, an implicit scalar-field approach is adopted, in which fiber trajectories are represented by the iso-contours of a scalar function φ. The scalar field is optimized such that its gradient is orthogonal to the principal-stress direction and its magnitude matches the desired local path density. This formulation unifies trajectory orientation and density modulation within a single optimization framework, ensuring numerical stability and geometric smoothness of the extracted fiber paths.

During optimization, an energy functional Φ is defined as the overall objective, incorporating stress-orientation alignment, density consistency, and boundary-continuity regularization terms and manufacturability-related constraints. Minimization of these functional yields a continuous and curvature-constrained path distribution. The comprehensive objective function is expressed as:

$$\Phi = \int \left[\omega_1 \left\| \nabla\varphi \cdot \tau \right\|^2 + \omega_2 \left(\left\| \nabla\varphi \right\| - \rho_r r_d \right)^2 + \omega_3 p_c + \omega_4 b_c + \omega_5 \left(B_{target}(x) - b(x) \right)^2 \right] d\Omega \tag{1}$$

where τ is the principal-stress direction, ρ_r is the target path density, r_d is the length-distortion coefficient, p_c and b_c are penalty terms for path closure and boundary continuity, respectively, $B_{targe}(x)$ is the prescribed local ventilation target field, and $b(x)$ is the local porosity indicator induced by the scalar-field gradient.

In this formulation, each weighting factor governs an independent physical requirement embedded in the scalar-field optimization framework. The term weighted by ω_1 enforces alignment between the extracted fiber trajectories (iso-contours of φ) and the principal stress direction τ, thereby promoting stiffness-oriented reinforcement along dominant load-transfer paths. The coefficient ω_2 regulates the magnitude of $\|\nabla\varphi\|$ to achieve stress-adaptive path density after compensation by r_d, ensuring appropriate material distribution across regions with varying stress intensity. The penalty terms weighted by ω_3 and ω_4 suppress undesired closed loops and maintain boundary continuity on closed-shell surfaces, thereby preserving manufacturability and geometric coherence. The ventilation-related term weighted by ω_5 penalizes the mismatch between the desired local ventilation distribution and the actual porosity distribution induced by path density, thereby enabling spatially resolved coordination between structural reinforcement and breathability. All energy terms were first normalized to eliminate differences in dimension and magnitude, and ω_1-ω_5 were then tuned through sensitivity analysis to balance mechanical performance, manufacturability, and ventilation. The final weights were selected as the set that satisfied path continuity and manufacturing constraints while providing improved ventilation.

Building upon this framework, a locally varying ventilation target field is introduced. To reflect the design principle that low-stress regions should be more breathable whereas high-stress regions should remain denser, a normalized stress measure is first defined as:

$$\tilde{\sigma}(x) = \frac{\sigma(x) - \sigma_{\min}}{\sigma_{\max} - \sigma_{\min}},\ B_{target}(x) = 1 - \tilde{\sigma}(x) \tag{2}$$

where $\sigma(x)$ denotes the scalar stress-intensity measure obtained from FEA, and $\sigma_{\min}$ and $\sigma_{\max}$ are the minimum and maximum values within the design domain. Under this definition, $B_{\text{target}}(x) \in [0,1]$: regions with higher stress are assigned lower target ventilation values, while regions with lower stress are assigned higher target ventilation values. This continuous mapping avoids abrupt partitioning between solid and porous zones and provides a smooth target field for graded structural design.

To characterize the actual local porosity induced by the optimized scalar field, a local ventilation indicator is defined as:

$$b(x) = \mathcal{H}(\rho_{th} - \|\nabla\varphi(x)\|) \tag{3}$$

where $\mathcal{H}(\cdot)$ denotes a smooth Heaviside function and ρ_{th} is a density threshold distinguishing porous and solid-dominated regions. Accordingly, the ventilation penalty term can be written as:

$$\mathrm{E_b} = \int_{\Omega} (\mathrm{B_{target}}(x) - b(x))^2 \mathrm{d}\Omega \tag{4}$$

This term drives the optimized path-density field to approach the target ventilation distribution pointwise over the domain. As a result, low-stress regions are gradually sparsified to improve ventilation, while high-stress regions remain relatively dense to preserve load-transfer continuity and structural stiffness. Because both $B\text{target}(x)$ and $b(x)$ vary smoothly in space, the resulting porosity transition is continuous and does not introduce abrupt stiffness discontinuities.

Fiber paths are extracted as varying-height contours from the optimized scalar field φ. The spacing between these contours determines the fiber density and, consequently, the structural performance. To ensure manufacturability, constraints on inter-path spacing and turning radius are applied, and segments violating the minimum curvature or spacing criteria are excluded when extracting iso-contours.

Specifically, the local inter-path spacing is defined as:

$$s(x) = \frac{1}{\|\nabla\varphi(x)\|} \quad with\ s(x) \geqslant f_w \tag{5}$$

where $s(x)$ denotes the local spacing between adjacent paths, $\nabla\varphi(x)$ is the scalar-field gradient, and f_w represents the effective filament width. This constraint prevents overlap and excessive material accumulation during deposition.

In addition, a geometric curvature constraint is imposed to avoid excessively sharp turning during continuous fiber placement:

$$\kappa(x) = \left\| \frac{d^2 r}{ds^2} \right\| \leqslant \kappa_{\max} = \frac{1}{R_{\min}} \tag{6}$$

where $\kappa(x)$ denotes the curvature along arc length s, and R_{min} is the minimum allowable bending radius determined by filament stiffness and nozzle geometry. This constraint reduces the risk of fiber fracture, lifting, or nozzle clogging during multi-axis deposition.

After uniform resampling and smoothing, the resulting curves are connected into a single continuous toolpath following a one-stroke strategy. For the finger-splint geometry considered in this study, the stress-guided path-generation procedure is completed offline prior to fabrication and requires only modest computational effort, introducing no noticeable delay relative to the subsequent printing process. Trajectory smoothing is further applied at corner transitions to ensure gradual directional variation, thereby improving interlayer contact stability and reducing localized delamination risk.

Once path generation is completed, the optimized fiber layout is mapped back onto the three-dimensional surface and translated into a printable trajectory through multi-axis posture planning. The tangent direction of each path defines the feed orientation, while the surface normal constrains the nozzle attitude; their relative orientation is adjusted in real time via inverse kinematics to maintain fiber tension and deposition stability. Under this local pose constraint, the nozzle remains aligned with the surface normal and maintains a controlled stand-off distance from the substrate, thereby reducing the risk of nozzle–surface collision during multi-axis deposition. In addition, the previously defined inter-path spacing and curvature constraints inherently limit excessive lateral deviation and abrupt turning, further minimizing potential tool–path interference without requiring a separate global collision-detection routine.

To ensure reliable interlayer bonding, the splint structure is fabricated using a dual-layer deposition strategy. The first layer serves as a conformal structural substrate attached to the mold surface, while the second layer is deposited directly on top of it following the optimized fiber paths. During deposition, the molten PLA matrix partially remelts the underlying layer, enabling molecular diffusion and mechanical interlocking across interfaces. After printing, specimens undergo secondary thermal treatment at 80 °C for 3 h, further enhancing interlayer adhesion and fiber–matrix bonding strength by relieving residual thermal stress and improving interfacial contact.

The control system synchronizes extrusion rate and motion velocity to ensure continuous material flow on curved surfaces without dragging or over-deposition. Considering the brittleness of basalt fiber and the viscoelastic nature of PLA, a minimum curvature radius and a maximum turning-rate constraint are imposed in the path-planning phase to prevent filament fracture or nozzle clogging. Finally, the toolpath data are smoothed and velocity-synchronized before being executed by the robotic arm, completing the printing process.

3. RESULTS AND DISCUSSION

3.1 Stress-Guided Fiber Path Generation and Printing Implementation

To achieve stress-oriented reinforcement and lightweight design for rehabilitation splints, a representative loading model of the finger joint was first established. This model can be approximated as a three-point bending configuration, where the joint center is subjected to an upward bending load and both ends are constrained. Based on this condition, finite element analysis (FEA) was conducted to obtain the equivalent stress distribution of the finger-splint structure, as shown in FIGURE 4(A).

To ensure consistency between numerical modeling and the stress-guided design formulation, the BF/PLA composite was represented using equivalent homogeneous isotropic material parameters in the finite element analysis. The primary objective of the simulation is to resolve principal stress trajectories that govern fiber path alignment within the stress-driven optimization framework. Under bending-dominated loading, principal stress orientations are predominantly determined by structural geometry and boundary conditions. Accordingly, this material representation provides a stable and physically coherent stress-field foundation for stress-guided path generation, while preserving the dominant load-transfer characteristics of the splint structure.

The results indicate that the maximum equivalent stress occurs at the dorsal midsection of the splint, corresponding to the region of maximum bending moment during finger flexion, thereby providing the basis for subsequent fiber alignment and localized structural enhancement.

The stress tensor field obtained from FEA was converted into a continuous vector field representing the principal stress gradient direction, as shown in FIGURE 4(B). Using a quasi-conformal mapping method, this field was projected onto a two-dimensional parameter domain while preserving local angular continuity and minimizing length distortion. In the flattened domain, continuous fiber paths were generated along the maximum principal stress gradient, producing the streamline distribution shown in FIGURE 4(C). A regional density function was introduced to adjust local fiber density according to stress magnitude: dense in high-stress regions for reinforcement and sparse in low-stress regions to form ventilation channels. This density modulation allows the fiber layout to achieve both mechanical strengthening and improved breathability.

To improve in-plane continuity and structural stability, an orthogonal path set was superimposed on the principal trajectory field, achieving bidirectional reinforcement, as shown in FIGURE 4(D). A single-stroke algorithm was applied to connect discrete streamlines into a continuous path, avoiding interruptions or redundant overlaps and ensuring smooth and uninterrupted material deposition. The algorithm preserves directional consistency with the principal stress field while allowing local openings in sparse regions, thereby balancing structural integrity with air permeability.

After completing the path planning, the two-dimensional trajectories were remapped onto the three-dimensional curved surface model to obtain the complete spatial fiber configuration, as illustrated in FIGURE 4(E). During this mapping process, sparse regions appeared as distributed mesh-like pores over the curved surface, forming breathable patterns consistent with the stress gradient distribution. The final printing process was performed on the multi-axis additive manufacturing platform, and the fabricated specimen is shown in FIGURE 4(F). The printed fibers exhibit uniform orientation and continuous connection, with open regions aligning closely with the simulated stress field. The resulting structure provides the required load-bearing stiffness while forming an orderly ventilation network.

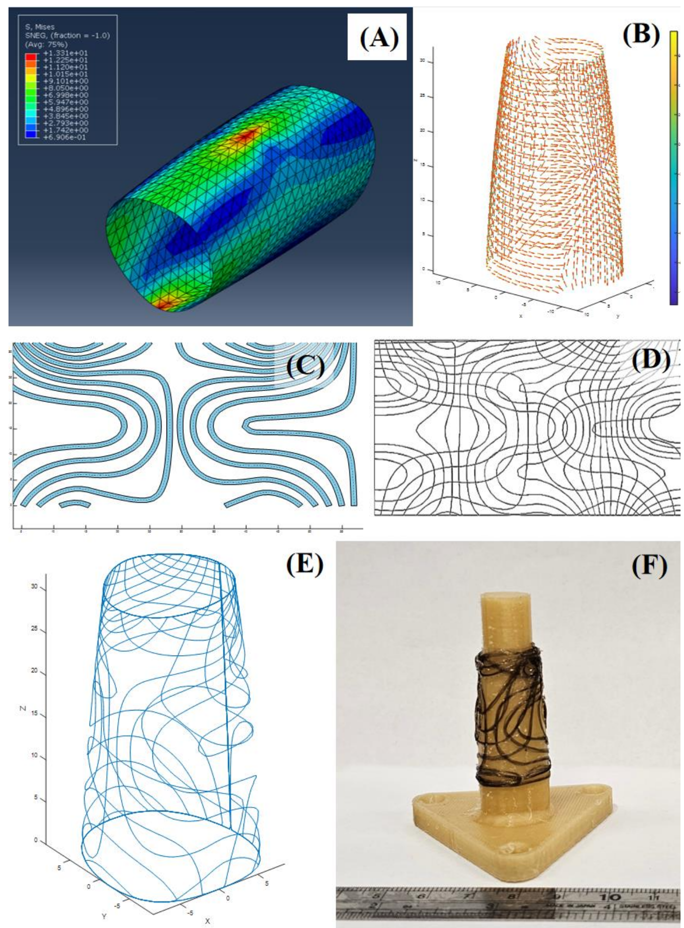

FIGURE 4: STRESS-GUIDED FIBER-PATH GENERATION AND PRINTING PROCESS. (A) FEA STRESS DISTRIBUTION OF THE FINGER-SPLINT MODEL; (B) PRINCIPAL STRESS VECTOR FIELD; (C–D) 2D PATH GENERATION AND ORTHOGONAL CONNECTION; (E) 3D REMAPPED FIBER LAYOUT; (F) PRINTED PROTOTYPE WITH CONTINUOUS AND BREATHABLE FIBER DEPOSITION.

3.2 Performance Comparison and Analysis

To evaluate the mechanical performance of the optimized structure, three types of samples were fabricated for comparison: Dense Composite (DC): densely deposited basalt fiber reinforced PLA composite; Optimized Composite (OC): stress-guided sparse composite structure generated by the optimization algorithm; Dense PLA(DP): densely deposited pure PLA specimen, as shown in TABLE 3.

TABLE 3: Morphology of the three types of printed splint specimens.

Type of samples	Morphology
Dense Composite	
Optimized Composite	
Dense PLA	

Prior to structural-level bending validation, the intrinsic mechanical behavior of the printed composite material was characterized through standardized tensile testing of BF/PLA specimens [17]. The tensile modulus and strength parameters obtained along the primary reinforcement direction are summarized in Table 4. Compared with neat PLA, the BF/PLA composite exhibits a substantially higher tensile modulus, reflecting the effective load transfer provided by continuous basalt fibers. In addition, cross-sectional SEM micrographs of tensile fracture surfaces (Figure 5) reveal a continuous fiber distribution embedded within the PLA matrix and demonstrate characteristic failure features including brittle matrix fracture and localized fiber–matrix interfacial separation. These material-level observations establish the constitutive basis for interpreting the subsequent structural bending response of the splints.

TABLE 4: Material parameters of fiber and matrix material[17].

Parameter	PLA	BF/PLA
Diameter (mm)	1.75	1.6
Density (g/cm^3)	1.25	2.8
Elastic modulus E_1 (MPa)	2205.18	16322.17
Elastic modulus E_2 (MPa)	-	9930
Shear modulus G_{12} (MPa)	-	4138
Poisson ratio μ_{12}	0.36	0.2

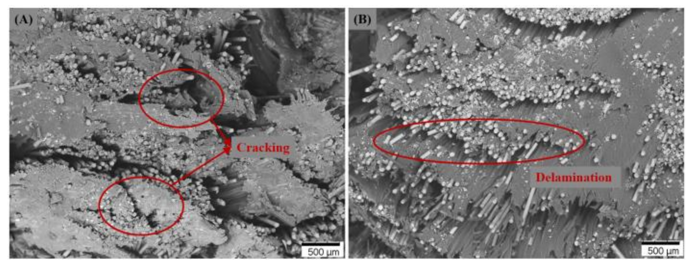

FIGURE 5: TENSILE FRACTURE CROSS-SECTIONAL MICROGRAPH.

All specimens were subjected to static three-point bending tests with a span of 20 mm, under a loading direction consistent with the simulated finger flexion condition.

The three-point bending configuration is adopted as a simplified mechanical representation of the dominant functional loading experienced by a finger splint during rehabilitation. In practical use, the primary function of the splint is to restrict joint motion, particularly flexion and extension around the articulation axis. This functional requirement leads to bending-dominated loading, as the splint resists angular displacement and rotation at the joint. Consequently, the internal stress state of the splint is largely characterized by tensile and compressive stresses distributed across its thickness, consistent with classical bending mechanics. Although in vivo loading conditions may involve additional complexity, bending resistance constitutes the primary structural demand during rehabilitation. Therefore, three-point bending provides a mechanically representative and reproducible approximation for evaluating stiffness and load-bearing capability under function-relevant conditions.

The experimental setup and samples are shown in FIGURE 6(A), and the corresponding force–displacement curves are presented in FIGURE 6(B). The typical load on the little finger during daily grasping or flexion activities ranges from 7 N to 10

N [18]. Therefore, 10 N was selected as the representative physiological load for performance evaluation.

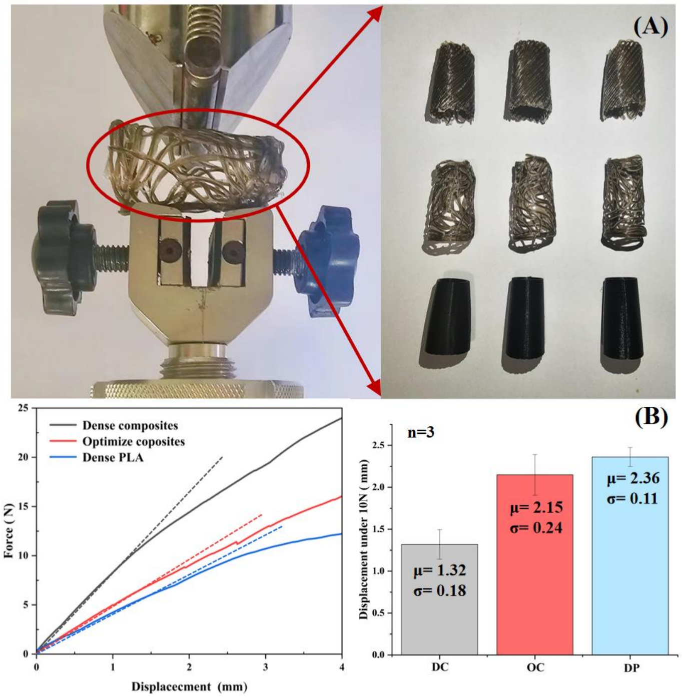

FIGURE 6: MECHANICAL PERFORMANCE COMPARISON OF DIFFERENT SPLINT STRUCTURES. (A) THREE-POINT BENDING TEST SETUP AND SAMPLES; (B) FORCE–DISPLACEMENT CURVES AND DISPLACEMENT AT 10 N.

Within this load range, none of the specimens exhibited fracture or interlayer delamination, demonstrating that all structures meet the basic strength requirements for rehabilitation splints. The DC specimen exhibited the highest bending stiffness, with a noticeably steeper force–displacement slope compared to the other two groups. Its stiffness was approximately 118 % higher than that of DP, confirming that the introduction of continuous basalt fibers significantly enhances the overall load-bearing capability. The OC specimen, although showing a 45 % lower stiffness than DC due to its sparser fiber layout, still exceeded DP by 19.9 %. This result indicates that the stress-guided sparse deposition effectively reduces material usage while maintaining sufficient mechanical performance. Fiber sparsification is introduced only in relatively low-stress regions and is governed by a continuous scalar-field-based density transition. This gradual redistribution avoids abrupt stiffness discontinuities, thereby preserving load-transfer continuity and mitigating the potential for local stress concentration or delamination.

At the reference load of 10 N, the displacement of the OC specimen was slightly larger than that of DC, yet far below the deformation threshold required for functional support. This confirms that its stiffness is adequate to restrict finger bending and prevent secondary injury during rehabilitation. Considering that the actual finger joint load rarely exceeds 10 N, the optimized structure provides sufficient support without causing discomfort associated with excessive rigidity.

All displacement values at 10 N are reported as mean ± standard deviation (n = 3 per group) in FIGURE 6. Statistical comparisons were performed using one-way ANOVA. The analysis revealed a significant difference among the three groups ($F(2,6) = 26.59$, $p < 0.05$), indicating that the variations in bending response are statistically meaningful.

In practical rehabilitation applications, splints are subjected to repeated flexion–extension cycles associated with daily joint motion. Under such service conditions, the structural response is governed not only by static stiffness but also by the stability of load transfer within the composite system over time. The continuous basalt fiber reinforcement forms aligned load-bearing paths along principal stress trajectories, which reduces localized matrix-dominated deformation and mitigates stress redistribution during repeated bending. From a micromechanical perspective, potential long-term degradation mechanisms may involve gradual matrix microcracking or localized interfacial separation; however, the substantially enhanced tensile modulus and stiffness contribution provided by the continuous fibers contribute to maintaining structural continuity and load-sharing efficiency. The stress-guided path distribution further avoids abrupt stiffness transitions, thereby reducing the likelihood of concentrated strain accumulation in low-stress regions. Collectively, these factors support the structural robustness of the optimized splint configuration under extended use scenarios.

Mass comparison results (TABLE 5) show that the OC specimen's mass was reduced by approximately 58.3% compared to DC, and by 28.6% relative to DP. The mass values are also presented as mean ± standard deviation (n = 3), and statistical analysis using one-way ANOVA confirmed significant differences among the three groups ($p < 0.05$), demonstrating that both material system and structural configuration contribute to statistically significant mass variations. This clearly demonstrates that the stress-guided optimization achieves significant weight reduction while maintaining structural adequacy. The reduced mass not only lessens wearing burden but also decreases material consumption and printing energy, contributing to overall sustainability.

TABLE 5 Mass of samples (n=3)

Types	Mean mass
Dense Composite(DC)	1.20±0.11g
Optimized Composite(OC)	0.50±0.08g
Dense PLA(DP)	0.70±0.05g

In addition to mechanical performance, breathability is a critical factor influencing the comfort of rehabilitation splints. Prolonged closed contact often causes skin moisture accumulation and thermal discomfort, reducing patient compliance. The proposed path optimization algorithm introduces sparse deposition in low-stress regions, generating intrinsic openings that balance mechanical strength and airflow.

To quantitatively evaluate breathability, the open-area ratio was calculated from the two-dimensional unfolded patterns as the ratio of void area to total surface area. The optimized model exhibited an approximately 45% increase in open-area ratio compared with the dense model. Distinct ventilation channels formed in low-stress regions, while continuous fiber reinforcement was maintained in high-stress zones, achieving a synergistic enhancement of strength and breathability.

From a heat and mass transfer perspective, an increase in effective open area reduces resistance to convective air exchange and mitigates barriers to water vapor diffusion, thereby promoting renewal of the microclimate beneath the splint. The stress-guided path sparsification strategy enhances air circulation and moisture transport without compromising the continuity of the primary load-bearing fiber network, establishing a clear structure–function coupling: dense reinforcement is preserved in regions of concentrated bending stress, while permeability is increased in low-stress areas, enabling simultaneous mechanical reliability and thermal–moisture comfort. Wearing comfort further depends on both material safety and local microclimate regulation; PLA is widely recognized as a biocompatible thermoplastic in medical and wearable applications, and basalt fibers exhibit chemical stability without inducing adverse skin reactions under normal contact conditions. Accordingly, the proposed design integrates structural ventilation and material-level biocompatibility to support long-term comfort during rehabilitation use.

Observations during actual fitting also confirmed that the optimized specimens exhibited regular openings around the bending zone and lateral surfaces, effectively promoting air circulation and improving thermal–moisture comfort. This structural feature is particularly beneficial for long-term wear, mitigating skin irritation and reducing bacterial growth, thereby enhancing user compliance and rehabilitation effectiveness.

In summary, the optimized composite structure satisfies practical load-bearing requirements while achieving reduced mass and improved breathability. Its stiffness remains superior to that of traditional PLA splints, demonstrating an effective balance among mechanical strength, comfort, and environmental sustainability.

Although the present study demonstrates the framework using a finger-splint geometry, the proposed stress-guided design methodology is not restricted to a specific anatomical scale or curvature condition. The optimization procedure is fundamentally driven by finite element–derived stress fields and geometric mapping, both of which are independent of a particular joint configuration. For joints exhibiting larger curvature variations or higher load demands, such as the wrist, the same computational pipeline can be applied by redefining boundary conditions and load cases to obtain the corresponding stress distribution. The quasi-conformal mapping and multi-axis path remapping strategies enable trajectory generation on complex three-dimensional surfaces while maintaining fiber continuity. Therefore, the method represents a generalizable design framework for fiber-reinforced rehabilitation devices, with scalability governed primarily by the loading scenario and geometric complexity rather than by intrinsic algorithmic limitations.

4. CONCLUSION

This study developed an integrated framework combining basalt fiber/PLA composites, stress-guided fiber-path optimization, and multi-axis additive manufacturing for personalized rehabilitation splints. The proposed method aligns continuous fibers along principal stress gradients while introducing controlled porosity, achieving a balance between stiffness, lightness, and breathability. Experimental results demonstrated that the optimized composite structure meets functional fixation requirements, reduces material consumption substantially, and enhances comfort through improved ventilation. This work provides a sustainable and effective strategy for next-generation, high-performance rehabilitation orthoses.

ACKNOWLEDGEMENTS

The authors acknowledge support from the Research Grants Council (RGC) of the Government of Hong Kong Special Administrative Region (HKSAR) with RGCECS Project (No. 26215824), HKUST research equipment development fund, and HKUST Bridge Gap Fund (BGF). The help from the funding agency and the other researchers is sincerely appreciated.

REFERENCES

[1] Schneider, S. P. Musculoskeletal injuries in construction: a review of the literature. Applied occupational and environmental hygiene, 16(11), 1056-1064, 2001.

[2] Hurley, M. V. The effects of joint damage on muscle function, proprioception and rehabilitation. Manual therapy, 2(1), 11-17, 1997.

[3] Agadeesh, P., Sanjay, M. R., Rajeshkumar, G., Kandasamy, J., Oladele, I. O., Madhu, P., & Siengchin, S.. Development of eco-friendly basalt filler reinforced poly (lactic acid) composites using an additive manufacturing: An experimental insights. International Journal of Biological Macromolecules, 311, 143698, 2025.

[4] Singha, K. A short review on basalt fiber. International Journal of Textile Science, 1(4), 19-28, 2012.

[5] Jamshaid, H., & Mishra, R. A green material from rock: basalt fiber–a review. The Journal of The Textile Institute, 107(7), 923-937 2016.

[6] Sim, J., & Park, C. Characteristics of basalt fiber as a strengthening material for concrete structures. Composites Part B: Engineering, 36(6-7), 504-512, 2016.

[7] Czigány, T., Vad, J., & Pölöskei, K. Basalt fiber as a reinforcement of polymer composites. Periodica Polytechnica Mechanical Engineering, 49(1), 3-14,2005.

[8] Jagadeesh, P., Rangappa, S. M., & Siengchin, S. Basalt fibers: An environmentally acceptable and sustainable green material for polymer composites. Construction and Building Materials, 436, 136834, 2024.

[9] Hassan, B. R., Manguri, A., Hussein, A. B., Corrado, A., Abdulrahman, P. H., Mohammed, L. M., ... & Hatim, L. A..

Experimental and numerical assessment of recycled plastic fibers on shear strength and behavior of reinforced concrete beams with basalt FRP bars. Engineering Structures, 330, 119942, 2025.
[10] Xu, W., Xu, H., Li, Q., Zhang, P., Yang, L., & Wang, W.. Stress-based continuous planar path planning for additive manufacturing. Advances in Engineering Software, 188, 103544, 2024.
[11] Tam, K. M. M., & Mueller, C. T. Additive manufacturing along principal stress lines. 3D Printing and Additive Manufacturing, 4(2), 63-81, 2017.
[12] Sales, E., Kwok, T. H., & Chen, Y. Function-aware slicing using principal stress line for toolpath planning in additive manufacturing. Journal of Manufacturing Processes, 64, 1420-1433 , 2021.
[13] Liu, T., Yuan, S., Wang, Y., Xiong, Y., Zhu, J., Lu, L., & Tang, Y. Stress-driven infill mapping for 3D-printed continuous fiber composite with tunable infill density and morphology. Additive Manufacturing, 62, 103374, 2021.
[14] Medeghini, F., Trabucchi, I., Brentana, G., Tiberti, G., Plizzari, G. A., & Mark, P. Tailoring SFRC to mechanical needs: Full-scale experiments with optimized hybrid SFRC composition and fiber alignment to stress path. Engineering Structures, 343, 121231, 2021.
[15] Tang, P., Zhao, X., Shi, H., Hu, B., Ding, J., Yang, B., & Xu, W. A review of multi-axis additive manufacturing: Potential, opportunity and challenge. Additive Manufacturing, 83, 104075, 2021.
[16] Kubalak, J. R., Wicks, A. L., & Williams, C. B. Exploring multi-axis material extrusion additive manufacturing for improving mechanical properties of printed parts. Rapid Prototyping Journal, 25(2), 356-362, 2019.
[17] Yang, Y., Xu, Z., & Duan, M. Evolving Stress-Guided Continuous Fiber Path Optimization for Multi-Axis Additive Manufacturing of Composite Shells. Additive Manufacturing, 105012, 2019.
[18] Banuvathy, R., & Varadhan, S. K. M. Distinct behavior of the little finger during the vertical translation of an unsteady thumb platform while grasping. Scientific Reports, 11(1), 21064, 2021.

